arXiv:1410.4581v1 [astro-ph.HE] 16 Oct 2014

The Shapes of Pulsar Radio Pulses in the Plane of the Sky

H.L. Hakobyan[1], V.S. Beskin[1,2*]

[1] *Moscow Institute of Physics and Technology, State University, Institutskii 9, Dolgoprudny, 141700 Russia*

[2] *Lebedev Physical Institute, Russian Academy of Sciences, Leninskii pr. 53, Moscow, 119991 Russia*

*W*ill be published in Astronomy Reports

Translated by D. Gabuzda

Abstract – The sizes of pulsar radio pulses in the plane of the sky are determined. This is important not only in relation to the possibility of directly resolving the radio pulses spatially, but also for verifying and placing constraints on existing theories of the radio emission. The shape of the pulse radio image and its variation as a function of the pulse phase for the extraordinary (X) and ordinary (O) modes are determined for the simple case of a dipolar magnetic field. Images are obtained for pulsars with various angles between their magnetic and rotational axes, and also for various model parameters, such as the height of the emission, the size of the emission region as a function of the height, and the Lorentz factor of the secondary plasma. It is shown that the size of the resulting image is appreciably smaller at the center of the pulse than at its edges.

* Email: beskin@lpi.ru

1. INTRODUCTION

In spite of the absence of a generally accepted, consistent theory for the coherent emission of radio pulsars, the fully workable hollow-cone model developed over the nearly half a century these objects have been studied is able to explain the main geometrical properties of the mean pulses [1, 2, 3]. This model is based on the hypothesis that the beam of the radio emission repeats the density profile of the secondary electron-positron plasma, whose creation should be suppressed near the magnetic axis, where the radius of curvature of the magnetic-field lines is appreciably higher than it is far from this axis [4, 5].

According to current ideas, the secondary plasma is created near the magnetic poles of the neutron star, where there is a strong longitudinal electric field. The primary particles accelerated by this field move along curved trajectories, emitting curvature radiation at the characteristic frequency $\omega_{\rm cur} \sim (c/R_{\rm c})\gamma^3$, which falls in the gamma-ray range ($R_{\rm c}$ is the radius of curvature and γ is the Lorentz factor of the particles). The next process in the chain is the conversion of gamma-ray photons into electron-positron pairs, $\gamma + B \to e^+ + e^- + B$, which becomes possible only in a curved magnetic field; photons moving along the magnetic field are not able to be transformed into electron-positron pairs [6].

We conclude that the birth of secondary particles will be suppressed in a linear magnetic field (more exactly, in a magnetic field with a large radius of curvature), since both the intensity of the curvature radiation and the direction of propagation relative to the magnetic field become small. Therefore, the density of secondary particles should be lower in the central region of a polar cap than at its boundary. The radio emission of pulsars is usually thought to be associated with outflowing plasma.

The structure of the radio-emission beam has been studied in considerable detail, both theoretically and observationally (see, e.g., [7, 8]). For example, the dependence of the mean-profile widths on the pulsar period P and the observing frequency ν has been derived from observations [9, 10]. These results showed that the radio emission should be generated at heights $R_{\rm m}$ of the order of 10–100R, where R is the radius of the neutron star. Much attention has been paid recently to the construction of a consistent theory for the propagation of waves

in the magnetosphere [11, 12, 13] that can explain the main polarization properties of the emission beam.

On the other hand, the shape of the radio signal in the plane of the sky has not been studied previously. The reason is that, even if the spatial size of the image is several tens of neutron-star radii (of the order of 10^7 cm), the corresponding angular size for the nearest pulsars (with distances of order 100 pc) is only 10^{-4} microarcseconds, which cannot be resolved by current instruments. Therefore, the only means by which it may be possible to estimate the linear size of the radiating region is through interstellar scintillation [14, 15, 16]. Even then, it is only possible to obtain upper limits in most cases. Only recently, with the launch of the "RadioAstron" space radio telescope [17] has the possibility of directly resolving the spatial images of radio pulsars become available. Therefore, we believe that the time has come to study this question in more detail. The main assumptions used to construct the spatial image of the pulse radio emission and the main parameters influencing the shape of the image are described in Section 2. Section 3 concerns the methods used to determine the shape of the image and its dependence on the pulse phase. Finally, Section 4 presents a discussion of the results obtained.

2. MAIN ASSUMPTIONS

We will now formulate the main assumptions used to construct a pulse radio image in the plane of the sky. Recall that the pulsar radio emission has two different polarization modes-ordinary (O mode) and extraordinary (X mode) [2, 3]. The X mode always propagates along a straight line, while the O mode deviates from the magnetic axis at small distances from the neutron star. As was shown in [18], this deviation angle depends on the frequency ν as $\nu^{-0.14}$. We will consider this in more detail below.

Clearly, the geometrical properties of the observed radiation will depend on the structure of the emission beam. For simplicity, we assumed that the radio emission beam repeats the profile of the plasma density at the surface of the polar cap, which we write in the form

$$n_{\rm e} = \lambda g(r_\perp) n_{\rm GJ},$$
$$r_\perp = r \sin\psi_{\rm m}. \tag{1}$$

Here, $\lambda \sim 10^3 \div 10^4$ is the multiplicity of the particle creation, $n_{\rm GJ} = \mathbf{\Omega B}/2\pi ce$ is the so-called Goldreich-Julian density, and the factor $g(r_\perp)$ models the structure of the hollow cone, where $r_\perp$ is the distance from the magnetic axis (ψmis the angle between the magnetic axis and the radius vector). For simplicity, we assumed everywhere that the magnetic field of the neutron star corresponds to the field of a point dipole (this is clearly valid for distances $R_{\rm m}$, much smaller than the radius of the light cylinder, $R_{\rm L} = c/\Omega$)and did not include the effects of aberration.

As we already noted, there is no generally accepted theory of the radio emission that could be used to determine $g(r_\perp)$. Therefore, as in [13], we used the one-parameter approximation

$$g(r_\perp) = \left[1 + \left(\frac{f_0 R_0}{r_\perp}\right)^5\right]^{-1} \exp\left(-r_\perp^2/R_0^2\right). \tag{2}$$

Here, $R_0(r) = (\Omega r/c)^{1/2} r$ is the distance from the magnetic axis to the last open field line, which depends on the radius vector r and determines the opening angle of the beam in the hollow-cone model. The exponential factor leads to a sharp drop in the radio intensity when $r_\perp > R_0$. The parameter f_0 ($0 < f_0 < 1$) specifies the inner radius of the beam cavity, $f_0 R_0$; i.e., there is no cavity when $f_0 = 0$. Thus, the function $g(r_\perp)$ determines the intensity of the emission at a given emission level $R_{\rm m}$.

Further, since the emission at a given frequency can be generated over a wide range of heights r, we used the following additional factor in the parametrization:

$$h(r) = \exp\left[-A\frac{(r - R_{\rm m})^2}{R_{\rm m}^2}\right]. \tag{3}$$

$R_{\rm m}$ and A are the second and third parameters of our problem, and enabled us to take into account the contributions of different heights. When $A \gg 1$, the emission is generated only in a narrow range of heights, $r \approx R_{\rm m}$.

Finally, the fourth key parameter is the width of the beam for each radiating element relative to the direction of the magnetic field, θ_0. We took this angle to be $\theta_0 = 1/\gamma$, where γ

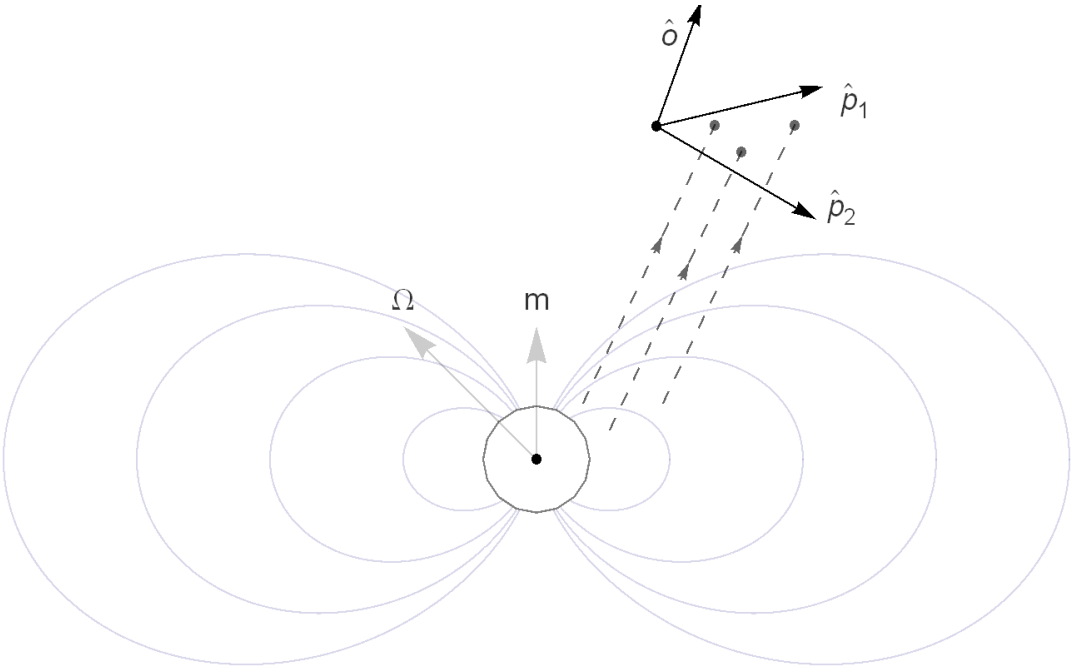

Fig. 1: Parallel rays that simultaneously intersect the screen (plane of the sky) in the direction toward the observer.

is the Lorentz factor of the outflowing plasma. In other words, we assumed that the emission intensity is proportional to

$$d(\theta) = \exp\left(-\gamma^2\theta^2\right), \tag{4}$$

where θ is the angle between the magnetic field and the direction of the beam propagation. As a result, the relative contribution of an element along a ray dl to the total intensity at the point $(r, r_\perp)$ (and for a ray propagating at an angle θ to the magnetic field) is proportional to $g(r_\perp)h(r)d(\theta)$.

3. CONSTRUCTION OF THE IMAGE IN THE PICTURE PLANE

Our task is to determine the emission intensity in the plane of the sky, i.e., for a distant "screen", for both the X mode and O mode. This reduces to calculating the integrated intensity along the trajectory of a ray passing through the screen at a point with coordinates (a_1, a_2)

along basis vectors $\hat{\mathbf{p}}_\mathbf{1}$ and $\hat{\mathbf{p}}_\mathbf{2}$ perpendicular to the fixed direction toward the observer, $\hat{\mathbf{o}}$ (Fig. 1). In this case, any point in plane of the sky can be represented

$$\mathbf{r}(a_1, a_2) = R_{\max}\hat{\mathbf{o}} + a_1\hat{\mathbf{p}}_\mathbf{1} + a_2\hat{\mathbf{p}}_\mathbf{2}, \tag{5}$$

where $R_{\max}$ is the distance of the screen from the center of the star (we assumed $R_{\max} = 1000R$). The intensity at a point with coordinates (a_1, a_2) can then be determined by integrating back along the ray trajectory,

$$I(a_1, a_2) = \int\limits_{\mathbf{r}(t)}^{R_{\max}} g(r_\perp)h(r)d(\theta)\mathrm{d}r \tag{6}$$

with fixed $\hat{\mathbf{o}}$, a_1, and a_2 at the surface of the screen. The image of a radio pulse in the plane of the sky for a given pulse phase ϕ can be obtained by carrying out the integration (6) along various rays that simultaneously pass through the screen surface in the direction toward the observer.

Clearly, in spherical coordinates with the z axis directed along the angular velocity $\mathbf{\Omega}$, we can write

$$\begin{aligned}
\hat{\mathbf{o}} &= \{\sin(\chi+\beta), 0, \cos(\chi+\beta)\},\\
\hat{\mathbf{p}}_\mathbf{1} &= \{\cos(\chi+\beta), 0, -\sin(\chi+\beta)\},\\
\hat{\mathbf{p}}_\mathbf{2} &= \{0, 1, 0\}.
\end{aligned} \tag{7}$$

Here and below, χ is the inclination of the magnetic- dipole axis $\mathbf{m}$ to the rotational axis $\mathbf{\Omega}$, and β is the minimum angle between $\hat{\mathbf{o}}$ and $\mathbf{m}$. For convenience, we introduced the dimensionless vectors $\hat{\mathbf{b}} = \mathbf{B}/B$, $\hat{\mathbf{m}} = \mathbf{m}/m$, and $\hat{\mathbf{n}} = \mathbf{r}/r$. In this case, the vectors that depend on the time t have the form

$$\begin{aligned}
\mathbf{m}(t) &= |\mathbf{m}|\{\sin\chi\cos(\phi+\Omega(t-t_0)), \sin\chi\sin(\phi+\Omega(t-t_0)), \cos\chi\},\\
\mathbf{B}(t) &= -\frac{\mathbf{m}}{r^3} + \frac{3(\mathbf{m},\hat{\mathbf{n}})\hat{\mathbf{n}}}{r^3}.
\end{aligned} \tag{8}$$

Naturally, determining the integral (6) requires knowledge of the ray trajectory $\mathbf{r}(t)$. In a

geometrical- optics approximation, we obtain

$$\begin{aligned} \frac{\mathrm{d}\mathbf{r}}{\mathrm{d}t} &= \frac{\partial\omega}{\partial\mathbf{k}} = c\,\frac{\partial}{\partial\mathbf{k}}\left(\frac{k}{n}\right), \\ \frac{\mathrm{d}\mathbf{k}}{\mathrm{d}t} &= -\frac{\partial\omega}{\partial\mathbf{r}} = -c\,\frac{\partial}{\partial\mathbf{r}}\left(\frac{k}{n}\right). \end{aligned} \tag{9}$$

For the linearly propagating X mode ($n \equiv 1$), we have simply

$$\begin{aligned} \frac{\mathrm{d}\mathbf{r}}{\mathrm{d}t} &= c\,\frac{\mathbf{k}}{k}, \\ \frac{\mathrm{d}\mathbf{k}}{\mathrm{d}t} &= 0, \end{aligned} \tag{10}$$

and, based on the initial condition (5), we can specify the trajectory as follows:

$$\begin{aligned} \mathbf{r}(t) &= (R_{\max} - ct)\hat{\mathbf{o}} + a_1\hat{\mathbf{p}}_\mathbf{1} + a_2\hat{\mathbf{p}}_\mathbf{2}, \\ \mathbf{k} &= \hat{\mathbf{o}} = \text{const}. \end{aligned} \tag{11}$$

The equations of motion are more complex in the case of the O mode, since the index of refraction n depends on the angle θ between the magnetic field and the wave vector $\mathbf{k}$ in a non-trivial way [18]:

$$n = 1 + \frac{\theta^2}{4} - \left(\frac{\theta^4}{16} + \theta_*^4\right)^{1/2}. \tag{12}$$

Here,

$$\theta_*^4 = \frac{\omega_\mathrm{p}^2}{\omega^2\gamma^3}, \tag{13}$$

where the plasma frequency

$$\omega_\mathrm{p}^2 = \frac{4\pi e^2 n_\mathrm{e}}{m_\mathrm{e}}, \tag{14}$$

will depend on the coordinate r through the particle number density

$$n_\mathrm{e} = \frac{\lambda}{2\pi ce} g(r_\perp)\,(\mathbf{\Omega B})\,. \tag{15}$$

As a test, Fig. 2 compares the numerical simulations for the dependence of the beam width W on the frequency ν for the case $g(r_\perp) = 1$, $R_\mathrm{m} = 10\,R$ and the analytical results obtained in [18] ($W = \text{const}$ for the X mode and $W \propto \nu^{-0.14}$ for the O mode). These are in very good agreement.

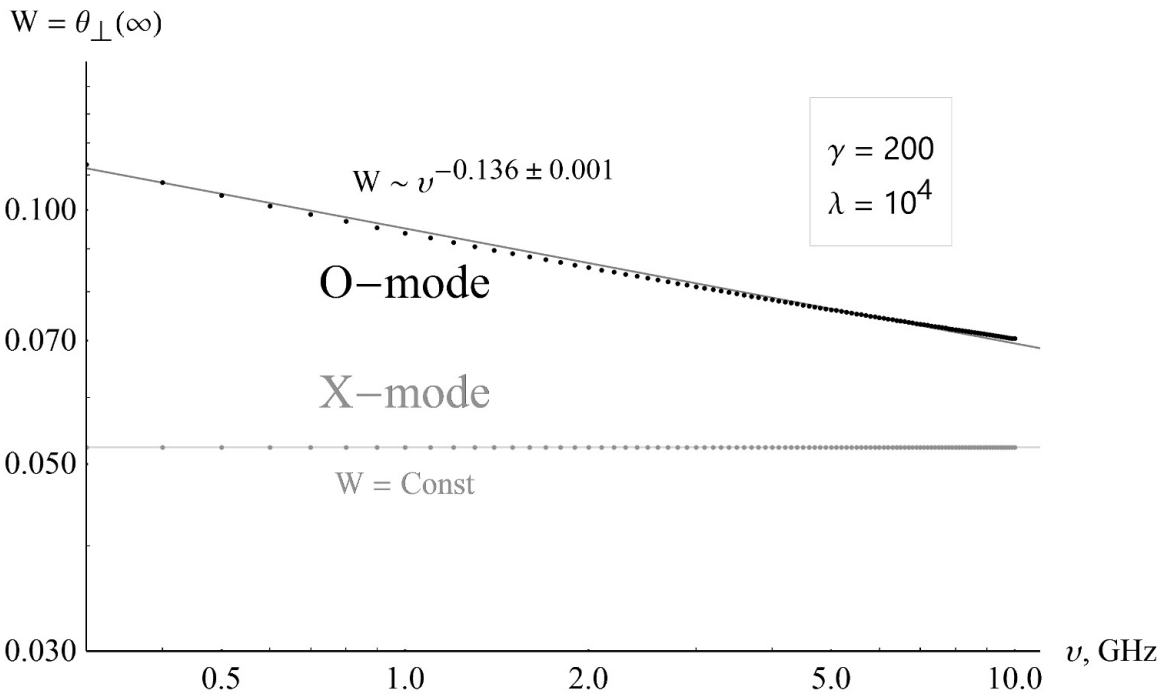

Fig. 2: Beam width W for the O and X modes for emission from a height of $R_{\rm m} = 10\,R$ for various frequencies ν.

4. DISCUSSION

As an example, Fig. 3 presents the motion of the image in the plane of the sky for the O mode from $\phi = -12^\circ$ to $\phi = 10^\circ$ for the case $\gamma = 100$. The linear dimensions are presented in units of the neutron-star radius R. Here and below, we have assumed $\beta = 5^\circ$, $\lambda = 10^4$, $\omega = 100$ MHz, $f_0 = 0.5$ and $P = 1$ s. The emission is slightly supressed at the pulse phase $\phi \approx 0^\circ$ due to the presence of the cavity f_0, however, this suppression is not stronger because the passage is not central and $\beta \neq 0^\circ$. On the other hand, we can clearly see that the image is strongly elongated at the edges of the mean profile. This is easy to understand. Consider the case when the magnetic axis is perpendicular to the rotational axis ($\chi = 90^\circ$), and the observer is located in the equatorial plane ($\beta = 0^\circ$). Since the emission occurs along magnetic-field lines, it can be received only from points that also lie in the equatorial plane. All the other field lines will deviate from the equatorial plane toward the North or the South, so that the emission from those points will not be detected. Consequently, in the limiting case

$\theta_0 = 1/\gamma \to 0$, the image in the plane of the sky will form a line lying in the equatorial plane, whose length depends on the emission level $R_{\rm m}$. It is obvious that this elongation will increase with increasing γ.

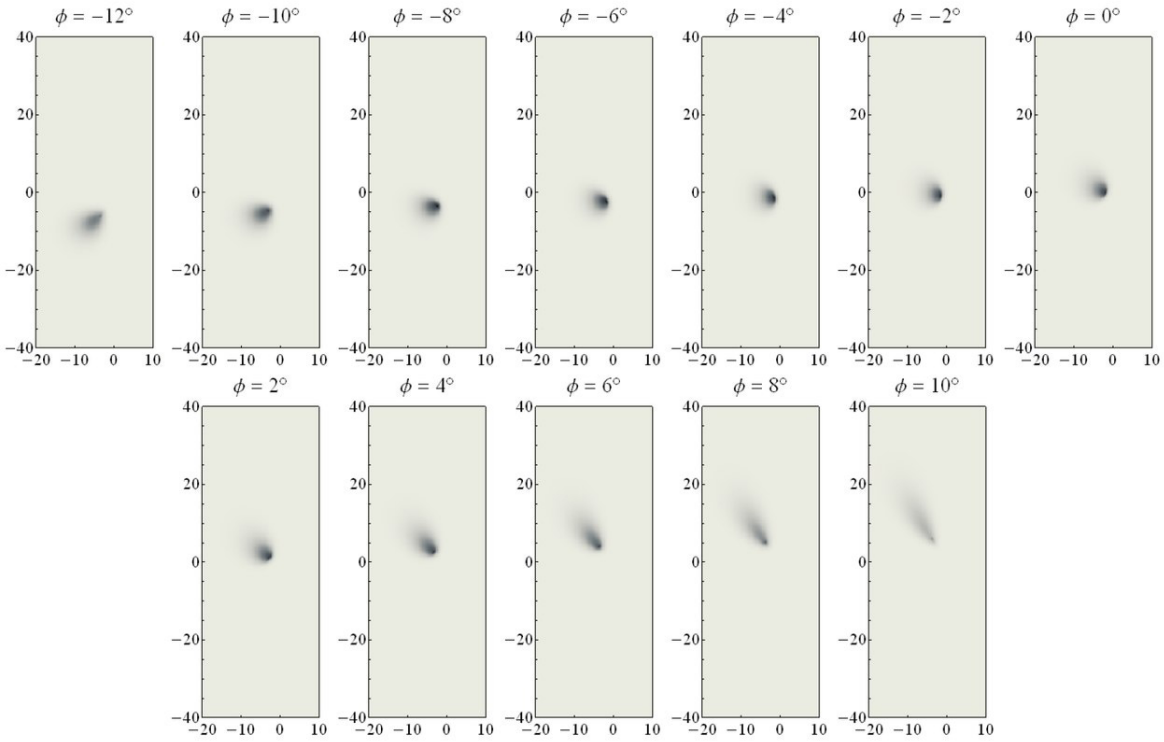

Fig. 3: Image of a radio pulse in the plane of the sky for $A = 0.1$, $R_m = 100$, $\chi = 45°$, and $\gamma = 100$. The sizes are shown in units of the neutron-star radius R.

For convenience of analysis, we present plots of various parameters obtained in our computations. The most important of these is the mean profile the dependence of the integrated intensity I on the phase ϕ. Another important characteristic is the dependence of the linear size of the image in the plane of the sky on the phase ϕ. We also present the trajectory of the intensity peak in the coordinates a_1 and a_2. Unless otherwise stated, $A = 0.1$, $\chi = 45°$, $\gamma = 50$, and $R_{\rm m} = 50$.

Figures 4 and 5 show the mean profile, image width, and motion of the image center for various values of A, for the O and X modes, respectively. The parameter A influences the width of the Gaussian (3), which specifies the dependence of the emission intensity on the

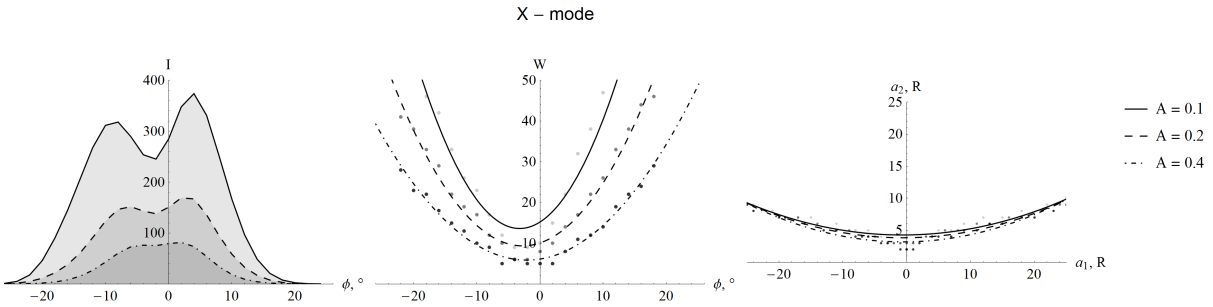

Fig. 4: Mean profile, image width, and motion of the image center for various values of A for the X mode.

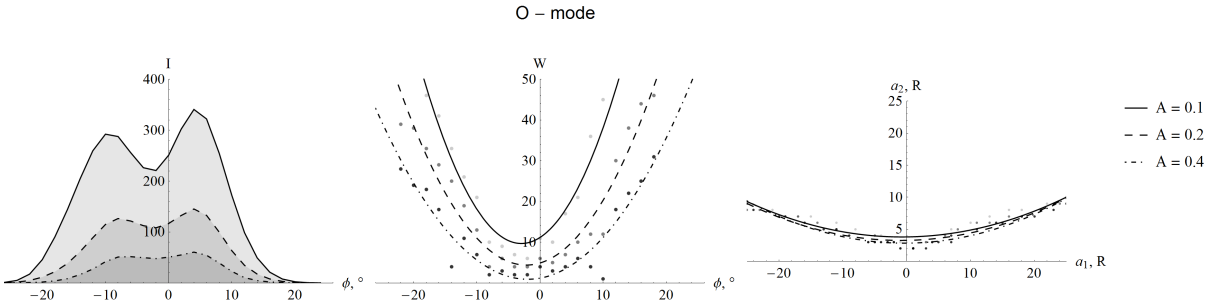

Fig. 5: Mean profile, image width, and motion of the image center for various values of A for the O mode.

height r, $h(r)$. As A is increased, this function becomes more degenerate, so that the emission emerges from a narrow layer at height $R_{\rm m}$. This leads to a low integrated intensity and a decrease in the profile width. In addition, the dependence of the image width on the phase ϕ becomes weaker as A is increased, since the image size is larger the more intense the emission at low heights. At the same time, the motion of the image center is virtually independent of A.

Figures 6 and 7 show the mean profile, image width, and image-center motion for various axis inclinations χ. As expected, this geometric factor strongly influences the width of the mean profile. When χ is small, the mean profile propagates over an appreciable part of the full period. On the other hand, when χ is close to 90°, the dependence of the image size on the phase ϕ strengthens, as is also obvious from geometrical arguments (the projection of the polar cap varies more strongly than for $\chi = 10°$). Finally, the motion of the image center depends

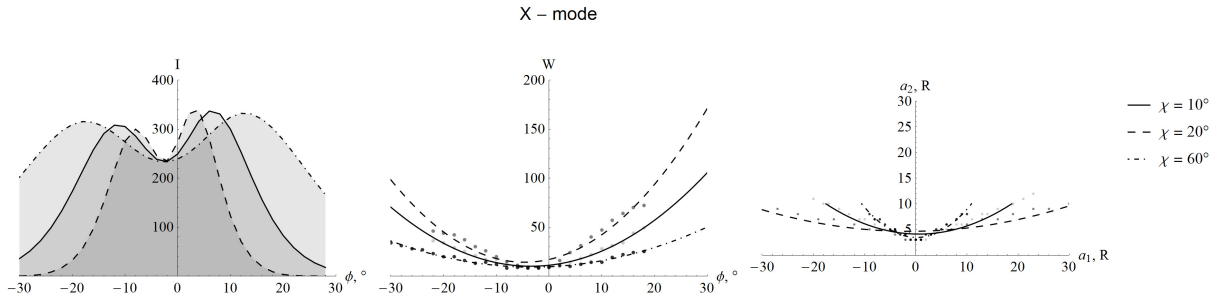

Fig. 6: Same as Fig. 4 for various axis inclinations χ.

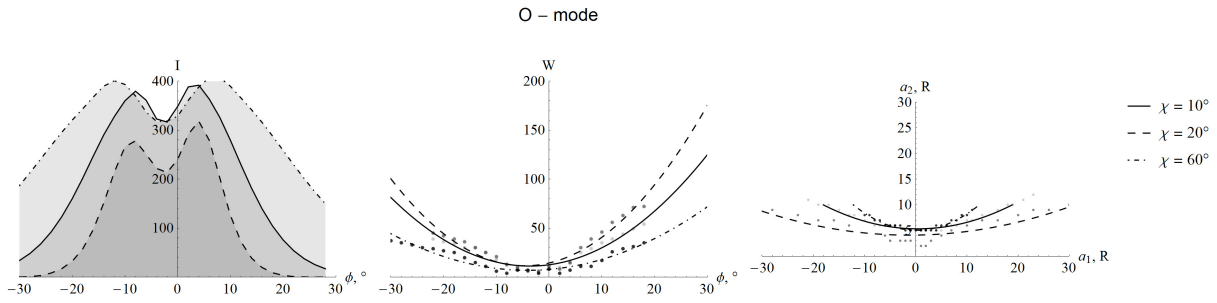

Fig. 7: Same as Fig. 5 for various axis inclinations χ.

strongly on χ. In the case of small inclinations, this trajectory degenerates into an elongated ellipse (the pulse is visible over the entire period), while it forms a line for inclinations close to 90°.

Figures 8 and 9 present the mean profile, image width, and image-center motion for various values of γ. In the profile and image-width plots, increasing γ has the same effect as increasing A: a decrease in the effective angle at which the radio emission is generated, causing the total intensity to fall. At the same time, as for A, the motion of the image center depends only weakly on γ.

Finally, Figures 10 and 11 show the mean profile, image width, and image-center motion for various values of $R_{\rm m}$. In the case of large $R_{\rm m}$ and $A = 0.1$, a wide band about $R_{\rm m}$ radiates, extending downward to R and upward to $10R_{\rm m}$. On the contrary, in the case of small $R_{\rm m}$, the radiation at high altitudes is suppressed. The pulsar radiates over a much wider interval of phase in the case of large $R_{\rm m}$. This gives rise to a sharp dependence of the image size on the height when $R_{\rm m} \sim 100\,R$. Again, the motion of the image center depends only weakly on $R_{\rm m}$.

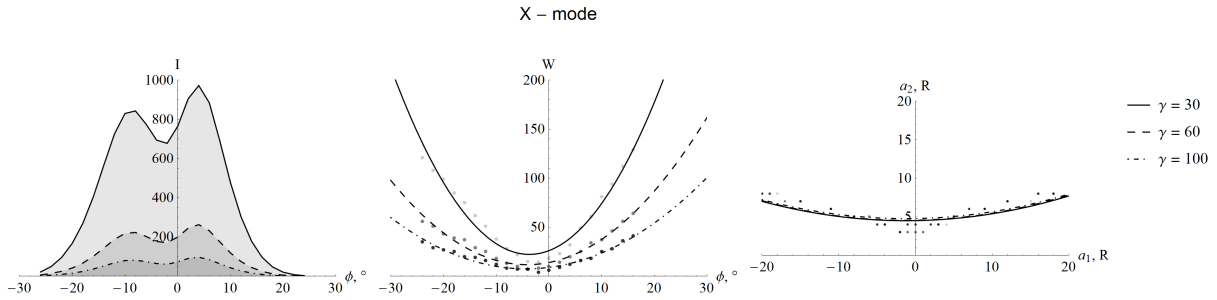

Fig. 8: Same as Fig. 4 for various values of γ.

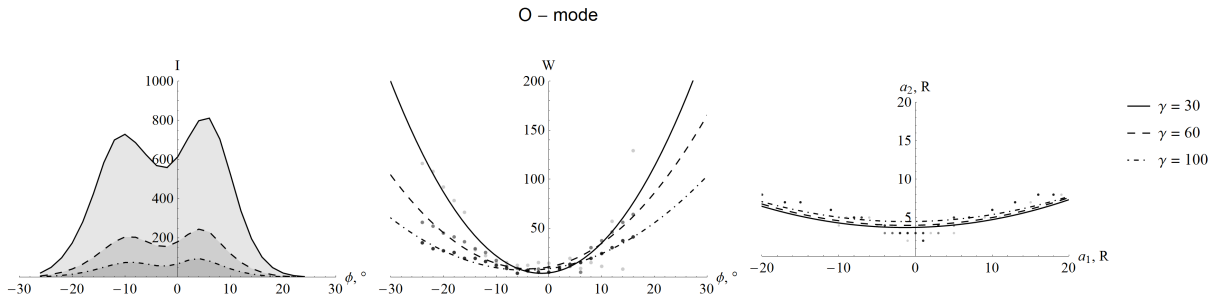

Fig. 9: Same as Fig. 5 for various values of γ.

Thus, even for fairly high emission heights $R_{\rm m} \sim 100\,R$, the size of the radio-pulse image does not exceed several neutron-star radii, of order 10^7 cm. It is therefore not surprising that it has not been possible to resolve pulsar images. However, our main conclusion that the size of the image at the center of the pulse should be appreciably smaller than at the pulse edges is supported by recent data on interstellar scintillation [19]. Finally, Pen et al. [20] have recently reported direct measurements of the velocity of a pulsar image on the plane of the sky of order 1000 km/s – close to the velocity with which the image moves in Fig. 3.

ACKNOWLEDGEMENT

The authors thank Ya.N. Istomin, Yu.Yu. Kovalev, M.V. Popov, and C.R. Gwinn for useful discussions. This work was supported by the Russian Foundation for Basic Research (project 14-02-00831).

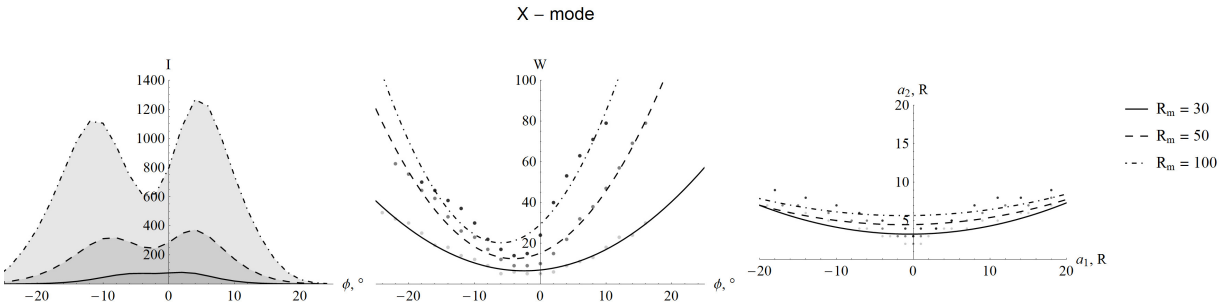

Fig. 10: Same as Fig. 4 for various values of $R_{\rm m}$.

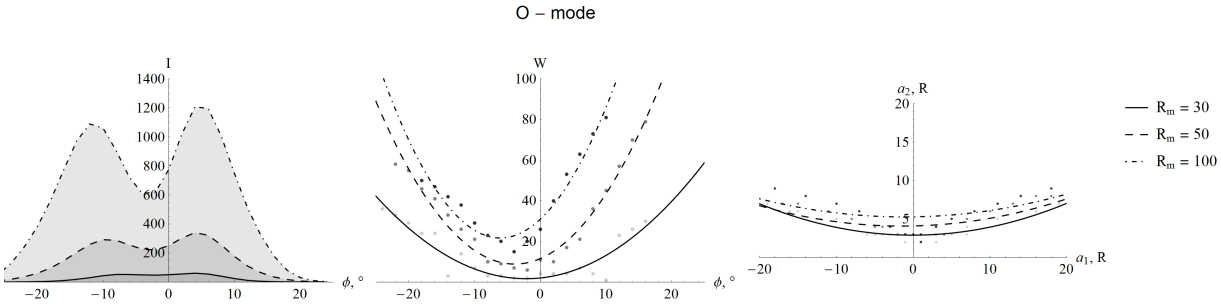

Fig. 11: Same as Fig. 5 for various values of $R_{\rm m}$.

REFERENCES

LITERATURE

[1] V. Radhakrishnan, D.J. Cooke, Astrophys. Lett. **3**, 225 (1969).

[2] F.G. Smith, *Pulsars*, (Cambridge Univ., Cambridge, 1977; Mir, Moscow, 1979).

[3] R.N. Manchester and J.H. Taylor, *Pulsars*, (Mir, Moscow, 1980; Freeman San Francisco, 1977).

[4] P.A. Sturrock, Astrophys. J. **164**, 529 (1971).

[5] M.A. Ruderman and P.G. Sutherland, Astrophys. J. **196**, 51 (1975)

[6] V.B. Berestetskii, E.M. Lifshitz, and L.P. Pitaevskii, *Course of Theoretical Physics, Vol.4: Quantum Electrodynamics*, (Fizmatlit, Moscow, 2002; Pergamon, Oxford, 1982).

[7] P. Weltevrede and S. Johnston, Mon. Not. R. Astron. Soc. **391**, 1210 (2008).

[8] T.H. Hankins and J. Rankin, Astron. J. **139**, 168 (2010).

[9] J.M. Rankin, Astrophys. J. **274**, 333 (1983).

[10] K. Maciesiak, J. Gil, and G. Melikidze, Mon. Not. R. Astron. Soc.**424**, 1762 (2012).

[11] S.A. Petrova and Y.E. Lyubarskii, Astron. Astrophys. **355**, 1168 (2000).

[12] C. Wang, D. Lai, and J. Han, Mon. Not. R. Astron. Soc. **403**, 2 (2010).

[13] V.S. Beskin and A.A. Philippov, Mon. Not. R. Astron. Soc. **425**, 814 (2012).

[14] C.R. Gwinn, N. Bartel, and J.M. Cordes, Astrophys. J. **410**, 673 (1993).

[15] T.V. Smirnova, V.I. Shishov, and V.M. Malofeev, Astrophys. J. **462**, 289 (1996).

[16] T.V. Smirnova, V.I. Shishov, and D. Stinebring, Astron. Rep. **75**, 866 (1998).

[17] N.S. Kardashev, Phys. Usp. **52**, 1127 (2009).

[18] V.S. Beskin, A.V. Gurevich, and Ya.N. Istomin, *Physics of the Pulsar Magnetosphere* (Cambridge Univ. Press, Cambridge, 1993).

[19] C.R. Gwinn, private commun. (2014).

[20] U.-L. Pen, J.-P. Macquart, A.T. Deller, and W. Brisken, Mon. Not. R. Astron. Soc. **440**, L36 (2014); arXiv:1301.7505v2 [astro-ph.HE](2013).